FULL PAPER

ADVANCED
ENERGY
MATERIALS

www.advenergymat.d

Check for updates

Li[Ni$_{0.9}$Co$_{0.09}$W$_{0.01}$]O$_2$: A New Type of Layered Oxide Cathode with High Cycling Stability

Hoon-Hee Ryu, Kang-Joon Park, Dae Ro Yoon, Assylzat Aishova, Chong S. Yoon,* and Yang-Kook Sun*

Substituting W for Al in the Ni-rich cathode Li[Ni$_{0.885}$Co$_{0.10}$Al$_{0.015}$]O$_2$ (NCA89) produces Li[Ni$_{0.9}$Co$_{0.09}$W$_{0.01}$]O$_2$ (NCW90) with markedly reduced primary particle size. Particle size refinement considerably improves the cathode's cycling stability such that the NCW90 cathode retains 92% of its initial capacity after 1000 cycles (compared to 63% for NCA89), while the cathode produces a high initial discharge capacity of 231.2 mAh g^{-1} (at 0.1 C). Thus, the proposed NCW90 can deliver high energy density and a long battery lifetime simultaneously, unlike other Ni-rich layered oxide cathodes. This unprecedented cycling stability is mainly attributed to a series of interparticular microfractures that absorb the anisotropic lattice strain caused by a deleterious phase transition near the charge end, thereby improving the cathode's resistance to fracture. Microcrack suppression preserves the mechanical integrity of the cathode particles during cycling and protects the particle interior from detrimental electrolyte attack. The proposed NCW90 cathode provides an improved material from which a new series of Ni-rich layered cathode can be developed for next-generation electric vehicles.

1. Introduction

Governments worldwide are increasingly adopting policies to replace internal combustion engine vehicles (ICEVs) with electric vehicles (EVs) in order to reduce CO$_2$ emissions, since transportation emissions account for nearly one-quarter of all greenhouse gases.[1] However, the current fleet of EVs, mainly powered by lithium-ion batteries (LIBs), still falls short of performance standards, especially in driving range per charge, that are required for broad consumer appeal. A driving range comparable to that of an ICEV requires a substantial increase in the energy density of LIBs, whose capacity is largely limited by the cathode.[2–4] Archetypal cathodes for LIBs deployed in current EVs are layered Li[Ni$_x$Co$_y$(Al or Mn)$_{1−x−y}$]O$_2$ (Al = NCA or Mn = NCM) oxide materials.[4–7] Both cathodes were derived from LiNiO$_2$, which has a high theoretical capacity of 270 mAh g^{-1}. Multiple phase transitions during delithiation quickly deteriorate the reversible capacity of LiNiO$_2$; this inherent structural instability renders the cathode unsuitable for EV applications. NCA cathodes were developed by introducing Co^{3+} and Al^{3+} to LiNiO$_2$ to prevent multistep phase transitions and stabilize the structure, resulting in the Li[Ni$_{0.8}$Co$_{0.15}$Al$_{0.05}$]O$_2$ cathode, which currently powers the Tesla Model S.[8] In another example, Ni was partially replaced with Co and Mn to develop Li[Ni$_{1/3}$Co$_{1/3}$Mn$_{1/3}$]O$_2$; this cathode exhibited excellent capacity retention and thermal stability but its capacity was limited to 160 mAh g^{-1}.[9] To compensate for inferior capacity, Ni content was increased to $x = 0.6$; this cathode is also widely commercialized. Although both NCA and NCM cathodes are adequate, the energy density of 350 Wh kg^{-1} required to provide a drive range threshold of 300 miles per charge requires a new class of layered oxide cathodes. As Ni content exceeds $x = 0.8$, NCA and NCM cathodes are plagued by increasingly compromised battery life and thermal safety, due to rapid capacity fading and an abundance of unstable Ni^{4+} species, as observed in LiNiO$_2$.[4,10–13]

To overcome the inherent instability of Ni-rich NCM and NCA cathodes, we propose a new type of layered oxide cathode, Li[Ni$_x$Co$_y$W$_{1−x−y}$]O$_2$. Previous work indicates that W doping of LiNiO$_2$ substantially improved its cycling stability without sacrificing energy density.[14,15] In this study, we show that replacement of Al ions with W ions in a Ni-rich NCA layered oxide cathode markedly modifies the cathode microstructure through particle refinement and greatly improves the cycling stability of the cathode. We compare the electrochemical performance of the Li[Ni$_{0.9}$Co$_{0.09}$W$_{0.01}$]O$_2$ cathode (NCW90) to the well-characterized Li[Ni$_{0.885}$Co$_{0.1}$Al$_{0.015}$]O$_2$ (NCA89) to demonstrate its superior structural and thermal stability compared to the commercialized NCA cathode.

H.-H. Ryu, K.-J. Park, D. R. Yoon, A. Aishova, Prof. Y.-K. Sun
Department of Energy Engineering
Hanyang University
Seoul 04763, South Korea
E-mail: yksun@hanyang.ac.kr
Prof. C. S. Yoon
Department of Materials Science and Engineering
Hanyang University
Seoul 04763, South Korea
E-mail: csyoon@hanyang.ac.kr
Prof. Y.-K. Sun
Department of Chemical Engineering
Hanyang University
Seoul 04736, South Korea

ADVANCED
SCIENCE NEWS
www.advancedsciencenews.com

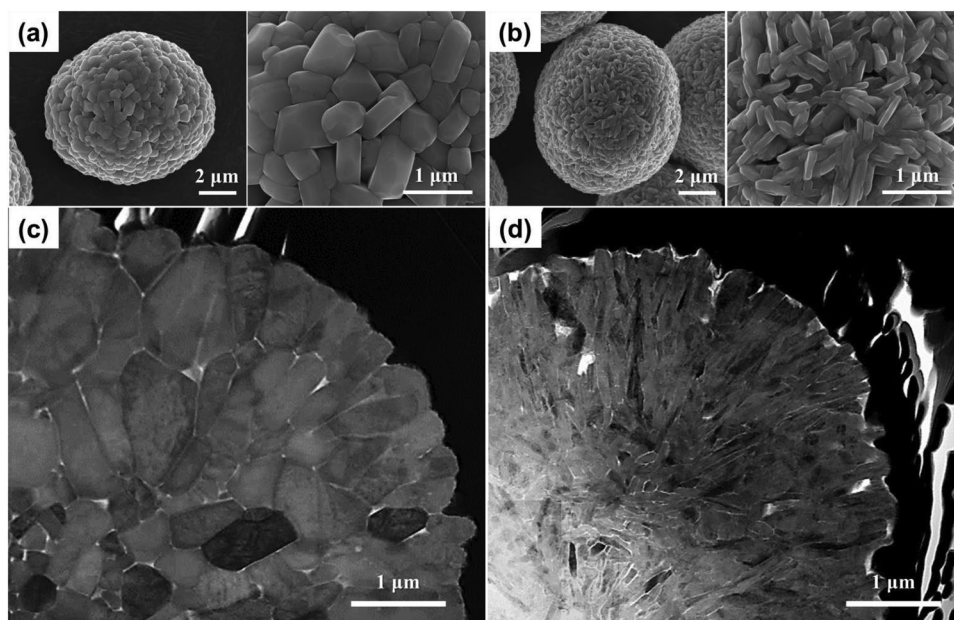ADVANCED
ENERGY
MATERIALS
www.advenergymat.de

Figure 1. SEM images with two different magnifications for a) NCA89 and b) NCW90 cathode particles. Bright-field STEM images show part of the particle cross-section for c) NCA89 and d) NCW90.

2. Results and Discussion

Scanning electron microscopy (SEM) images of the NCW90 and NCA89 cathode particles (shown in **Figure 1**a) indicate that both cathode particles are spherical in shape with an average particle diameter of 9–10 µm. Each particle is composed of nanosized primary particles. A striking difference in the size and the shape of the primary particles is observed although the precursor for the two cathodes prior to lithiation was nearly identical both in size and in shape (Figure S1, Supporting Information). While the NCA89 primary particles are ≈500 nm in size and nearly equiaxed in shape, the primary particles of the NCW90 cathode are elongated and much smaller, measuring less than 100 nm wide and ≈1 µm long. The bright-field scanning transmission electron microscopy (STEM) images in Figure 1c,d clearly show differences in the internal microstructures of the two cathode particles. The NCA89 cathode particle consists of relatively large randomly oriented primary particles, whereas the NCW90 cathode is composed of thin elongated primary particles arranged such that each primary particle appears to emanate from the particle center. Replacing Al with W slowed primary particle coarsening, which led to particle refinement. In addition, the presence of W ions modified the surface energy to increase anisotropy on different surfaces, leading to preferential growth direction and the observed needle-like primary particle morphology.

Rietveld refinement of the X-ray diffraction (XRD) data (**Figure 2**a and Figure S2, Supporting Information) shows that both cathodes have a rhombohedral layered structure (space group $R\bar{3}m$) without impurity phases. The calculated lattice parameters (Table S2, Supporting Information) suggest that the unit cell of the NCW90 cathode is slightly larger in both directions, likely due to the replacement of Al^{3+} (0.535 Å) with W^{6+} (0.60 Å).[16] Increased cation mixing observed in the NCW90 cathode was likely caused by increased Ni^{2+} concentration, which compensates
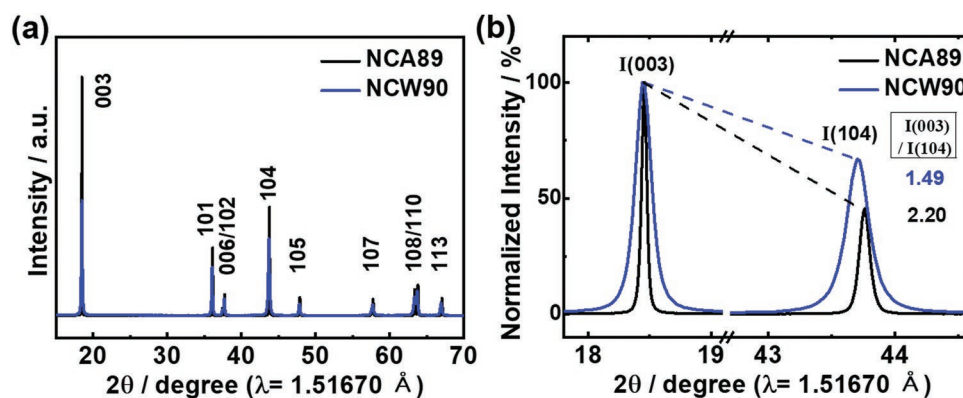

Figure 2. a) Powder XRD patterns for NCA89 and NCW90 from synchrotron radiation and b) comparison of the two patterns after normalization with their (003) peak intensities.
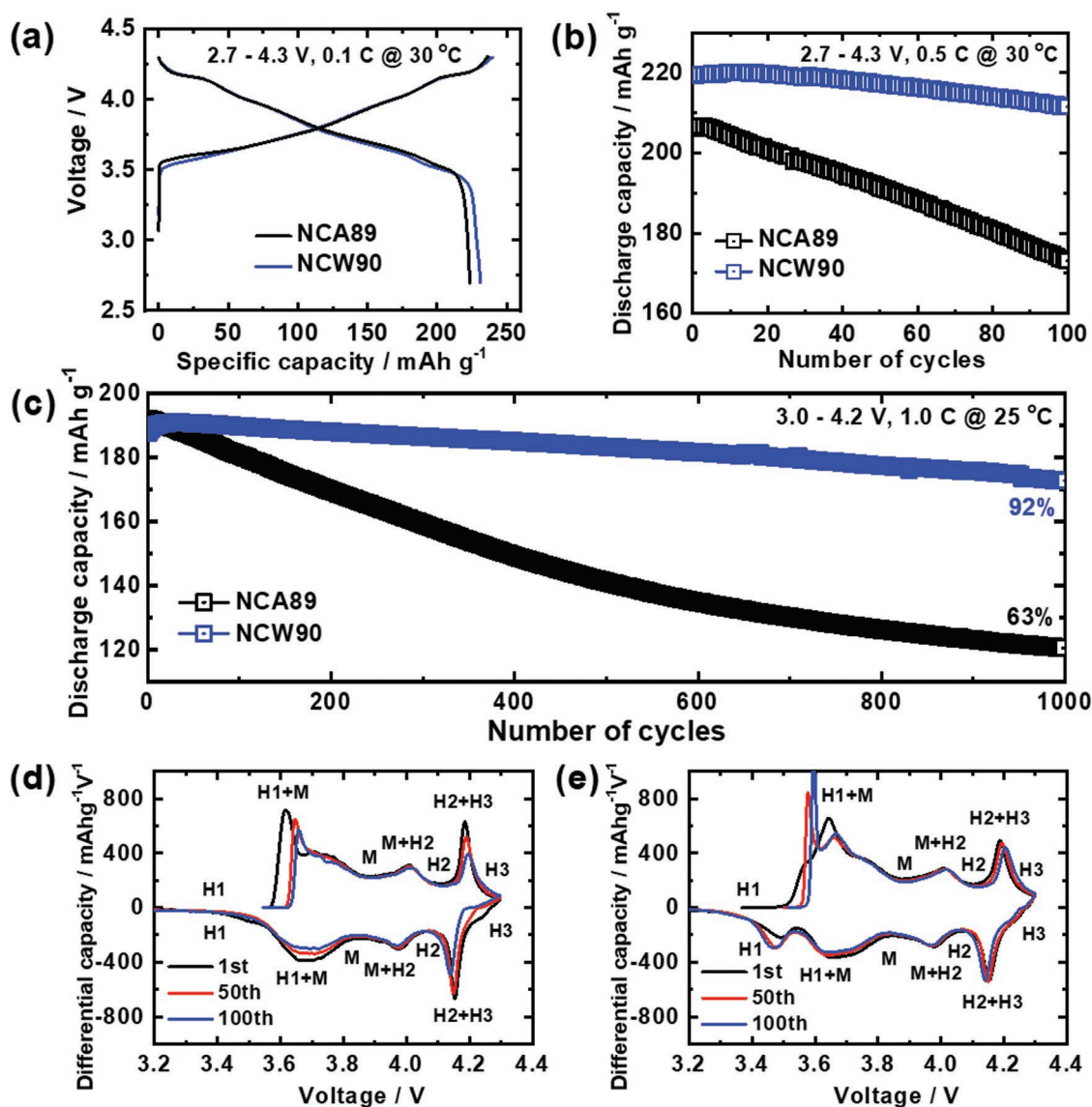
Figure 3. Comparison of the electrochemical performances for the NCA89 and NCW90 cathodes: a) initial charge–discharge curves at 0.1 C and 30 °C and b) cycling performances at 0.5 C and 30 °C between 2.7 and 4.3 V using 2032 coin-type half-cells with a Li metal anode. c) Long-term cycling performance of the NCA89 and NCW90 cathodes at 1 C and 25 °C between 3.0 and 4.2 V using pouch-type full-cells with a graphite anode. dQ dV^{-1} profiles obtained by differentiating charge–discharge curves at different cycle numbers for the d) NCA89 and e) NCW90 cathodes.

for the charge imbalance. Line broadening of the NCW90 XRD peaks in the magnified image (shown in Figure 2b) confirms the particle size refinement observed in the SEM and transmission electron microscopy (TEM) images of the NCW90 cathode.

Fundamental electrochemical performance of the NCA89 and NCW90 cathodes was characterized at 4.3 V using a 2032 coin-type half-cell with a Li metal anode. Because of nearly identical Ni content, the initial charge–discharge curves (at 0.1 C and 30 °C) (**Figure 3**a) show that both NCA89 and NCW90 cathodes produced similar discharge capacities with an initial cycle coulombic efficiency greater than 94%. The initial discharge capacity of 231.2 mAh g^{-1} at 0.1 C for the NCW90 cathode was slightly higher than that of the NCA89 cathode (223.5 mAh g^{-1}). Cycling performance was, however, markedly different. When

cycled at 0.5 C, the NCW90 cathode retained 96% of the initial capacity, while the NCA89 cathode retained only 83% after 100 cycles (Figure 3b). Thus, the NCW90 cathode was able to deliver a high discharge capacity like the NCA89 cathode while avoiding the capacity fading that plagues all Ni-rich NCA and NCM cathodes during cycling. The superior capacity retention of the NCW90 cathode is manifestly demonstrated in the full-cell cycling data shown in Figure 3c. The two cathodes were cycled in a pouch-type full-cell using a graphite anode at a rate of 1.0 C from 3.0 to 4.2 V (equivalent to 4.3 V vs Li) in a half-cell. The NCW90 cathode maintained 92% of the initial capacity even after 1000 cycles, whereas the capacity retention of the NCA89 cathode was limited to 63% during the same cycling period. The capacity retention of the NCW cathode is

**ADVANCED
SCIENCE NEWS**

www.advancedsciencenews.com

**ADVANCED
ENERGY
MATERIALS**

www.advenergymat.de

exceptionally high considering that an EV battery is typically guaranteed to retain 70% of the initial capacity after 8 years of service (1000 charge/discharge cycles are approximately equivalent to a battery life of ≈ 20 years with full charging weekly). In addition, a Ni-rich NCA cathode was able to maintain 80% of the initial capacity after 2000 cycles only if the available depth of discharge (DOD) was limited to 60%,[17,18] whereas the proposed NCW90 cathode achieved its exceptionally high capacity retention at full DOD.

To study the superior capacity retention exhibited by the NCW90 cathode, $dQ\ dV^{-1}$ profiles were calculated by differentiating the half-cell charge/discharge curves (Figure 3d,e). Both $dQ\ dV^{-1}$ profiles contain multiple peaks corresponding to the phase transitions incurred during charging (hexagonal (H1) → monoclinic (M) → hexagonal (H2) → hexagonal (H3)) and the transitions occurring in reverse order during discharging. The redox peaks for the NCA89 cathode showed noticeable changes in intensity, especially for the H2 ⇆ H3 phase transition, whereas the same redox peaks remained relatively stable for the NCW90 cathode. The decaying redox peaks in the $dQ\ dV^{-1}$ profile for the NCA89 cathode during cycling are an indication of deteriorating reversibility of the redox reactions, which is likely caused by the structural degradation of the cathode arising from the H2 ⇆ H3 phase transition. One of the main culprits for capacity fading in the Ni-rich layered cathodes (including LiNiO$_2$) is the abrupt lattice contraction and expansion associated with the H2 ⇆ H3 phase transition. LiNiO$_2$ experiences an abrupt reduction of ≈0.3 Å in the interlayer distance at the onset of the H2→H3 phase transition, disrupting the rechargeability of the cathode.[19] In fact, avoiding the H2→H3 phase transition enabled LiNiO$_2$ to cycle reversibly with a minimal capacity loss.[20]

To monitor the dimensional changes of the unit cell for the NCA89 and NCW90 cathodes during charging, in situ XRD measurements of the two cathodes were carried out while charging to 4.3 V at a constant current density of 36 mA g^{-1}. **Figure 4**a shows the c- and a-axis lattice parameters as a function of the state of charge. Both cathodes exhibit a similar dimensional change in the c-direction: an initial gradual expansion followed by abrupt contraction at about 4.2 V, corresponding to the onset of the H2→H3 phase transition. The maximum change in the c-axis lattice parameter for the NCA89 and NCW90 cathodes was nearly identical (−4.2% for NCA89 and −4.1% for NCW90) when charged to 4.3 V. For the a-axis lattice parameters, the unit cell continuously contracted in a similar manner and magnitude for both cathodes. The calculated unit cell volume (Figure 4b) indicates that lattice contraction was virtually identical for both cathodes; replacing Al by W in the NCA89 cathode affected the extent of detrimental lattice contraction minimally. However, despite similar levels of the lattice distortion at 4.3 V, the internal microstructure of the two cathodes was markedly different when charged to 4.3 V. The cross-sectional SEM images of the charged NCA89 cathode (Figure 4c) shows that it developed a network of microcracks emanating from the particle core when fully charged. Repeated opening and closing of such microcracks when charging and discharging, respectively, will eventually pulverize the cathode particle. In one severe case of microcracking, a portion of the secondary particle partially fractured during the first charge. In addition, these microcracks also provide pathways

for electrolyte infiltration and subsequent chemical attack of the crack faces, resulting in the formation of impedance-raising internal resistive surfaces during cycling.[21,22] In comparison, the charged NCW90 cathode sustained minimal structural damage with no major microcracks observed. Even if nucleated at the particle center, microcracks were arrested before reaching the particle surface in the NCW90 cathode. Microcrack suppression in the charged NCW90 cathode likely stemmed from the nanosized primary particles observed in the NCW90 cathode particle (Figure 1d). These nanosized primary particles partially dissipated the internal strain arising from the H2→H3 lattice distortion: numerous interparticle boundaries in the NCW90 cathode served as preferential sites for crack nucleation and propagation, releasing the strain energy. A similar enhanced fracture toughening is often observed in nanocrystalline ceramics.[23] Evidence for the interparticle boundaries in the NCW90 cathode acting as effective barriers for crack propagation can be clearly seen in Figure 4e,f. The microcracks in the NCA89 cathode tend to be straight due to the relatively large particle size, whereas the microcracks were short and zigzagged, tracing the interparticle boundaries. A similar observation was made in the STEM images of NCA89 and NCW90 cathode particle charged to 4.3 V (Figure 4g,h). Nearly all of interparticle boundaries in the charged NCA89 cathode were separated, forming a network of microcracks spanning from the particle core to surface while microcracks nucleated in the particle center in the charged NCW90 cathode were clearly suppressed through a series of interparticle fractures before reaching the particle surface. Therefore, the NCW90 cathode does not reduce the magnitude of lattice distortion observed in all Ni-rich layered cathodes in their highly delithiated state, but particle size refinement helped to negate the deleterious effect of the H2→H3 lattice distortion and to greatly improve the cathode's cycling stability.

The chemical stability of the NCW90 cathode was also verified by charge-transfer resistances, R_{ct}, estimated from the electrochemical impedance measured at intermittent intervals during cycling (**Figure 5**a and Figure S4, Supporting Information). In the NCA89 cathode, normal surface degradation from electrolyte attack leads to a continuous buildup of an impedance-increasing surface film; this buildup was aggravated by electrolyte infiltration through the particle interior, as evidenced by the sharp increase of R_{ct} as cycling proceeded. R_{ct} for the NCA89 cathode reached 59.2 Ω at the end of 100 cycles. Although surface-film (R_{sf}) and charge-transfer resistance for the NCW90 cathode were roughly equal during initial cycles (unlike that of the NCA89 cathode), R_{ct} for the NCW90 cathode did not increase markedly, reaching only 10 Ω after 100 cycles. The impedance data further substantiate that microcracking suppression in the fully charged state minimized electrolyte infiltration and protected the interparticle boundaries from electrolyte attack. In addition to the impedance data, the thermal stability of NCW90 was characterized using differential scanning calorimetry (DSC) of the charged cathodes (4.3 V) in the presence of the electrolyte solution (Figure 5b). The charged NCA89 cathode exhibited a large exothermic reaction peak at 192 °C, 10 °C below that of the NCW90 cathode. The heat released from the NCW90 cathode during the exothermic reaction was considerably less than that of the NCA89 cathode. The inhibition of microcracking, and thus the prevention of the
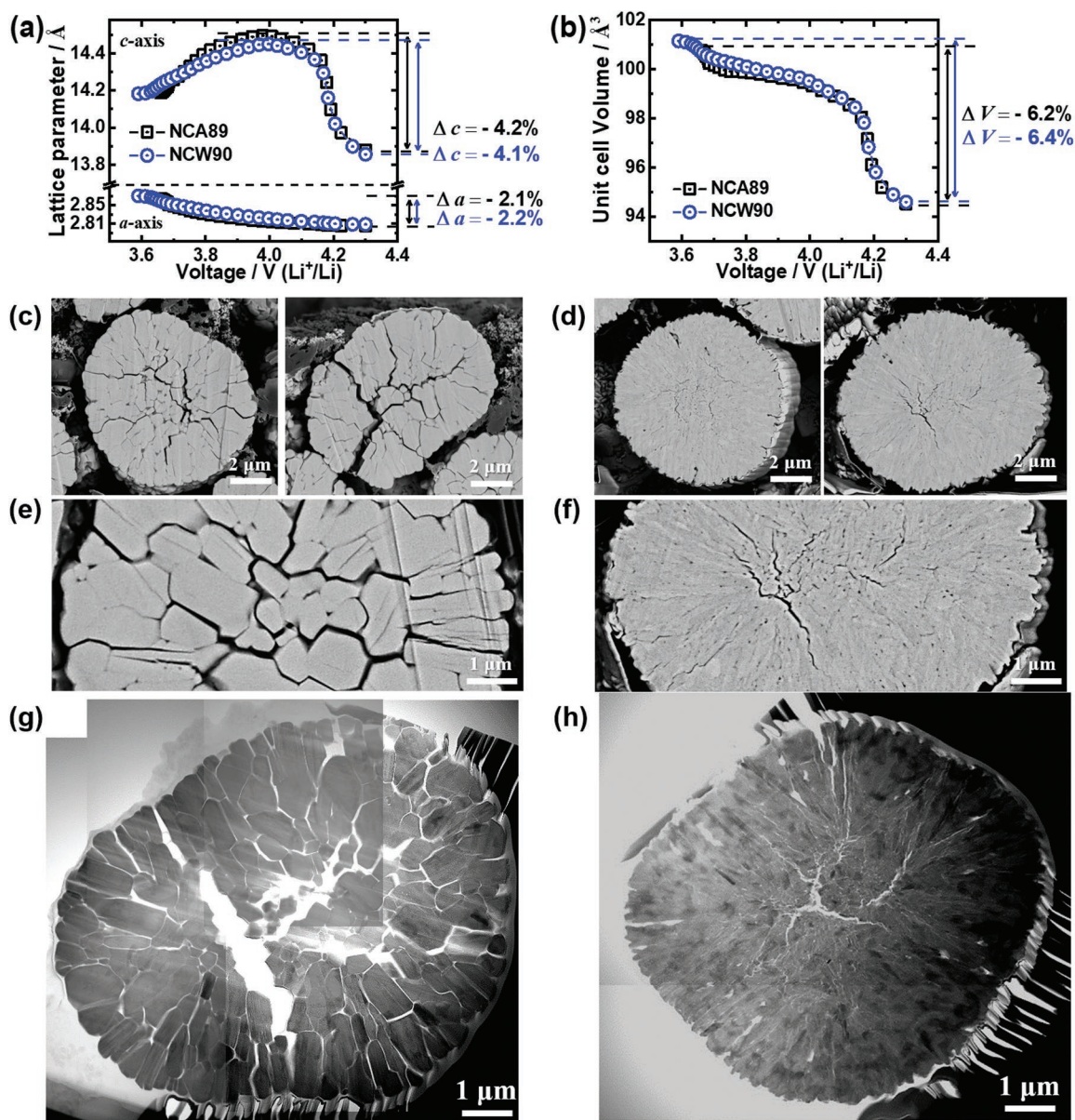
**ADVANCED
SCIENCE NEWS**
www.advancedsciencenews.com

**ADVANCED
ENERGY
MATERIALS**
www.advenergymat.de

Figure 4. Changes in a) *a*- and *c*-axis lattice parameters and b) unit cell volumes for NCA89 and NCW90 as a function of the cell voltage. Cross-sectional SEM images of c,e) NCA89 and d,f) NCW90 at fully charged states at 4.3 V. Bright-field STEM mosaic image of a cross-section of g) NCA89 and h) NCW90 at charged to 4.3 V.

penetration of the secondary particles by the electrolyte, largely reduced contact with the electrolyte and enhanced the thermal stability of the NCW90 cathode, producing superior mechanical and chemical stability of the NCW90 cathode.

3. Conclusion

Substituting W for Al in a Ni-rich NCA cathode greatly reduced the primary particle size. The observed particle size refinement remarkably improved the cycling stability of the cathode such that the NCW90 cathode retained 92% of the initial capacity after 1000 cycles while producing a high initial discharge

capacity of 231.2 mAh g^{-1} (at 0.1 C). The proposed NCW cathode represents a series of Ni-rich layered oxides that can deliver a high energy density and a long battery lifetime simultaneously, unlike NCA or NCM cathodes. The unprecedented cycling stability of the NCW90 cathode is mainly attributed to a series of interparticular microfractures that absorb anisotropic lattice strain caused by deleterious phase transitions near the charge end, thereby suppressing microcrack propagation and preventing cathode particle fractures. Microcrack suppression preserves the mechanical integrity of the cathode particles against abrupt lattice contraction and expansion during cycling and protects the particle interior from detrimental electrolyte attack. The proposed NCW90 cathode provides an improved
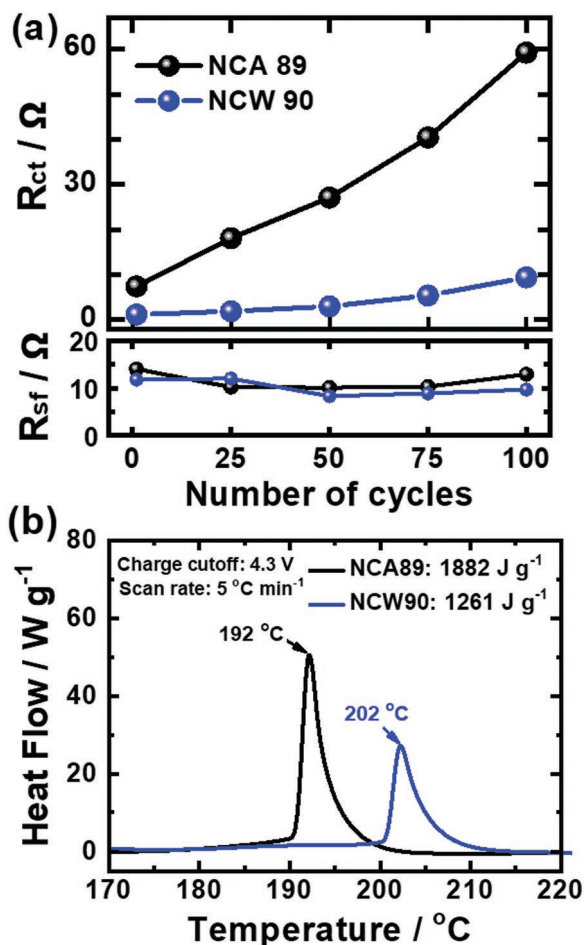
Figure 5. Comparison of a) the R_{sf} and R_{ct} changes measured every 25 cycles and b) DSC profiles for NCA89 and NCW90 in the delithiated state at 4.3 V.

material from which a new series of Ni-rich layered cathodes can be developed for next-generation EVs.

4. Experimental Section

Synthesis: Spherical $[Ni_{0.9}Co_{0.10}](OH)_2$ precursor was synthesized by a coprecipitation method. $NiSO_4 \cdot 6H_2O$ and $CoSO_4 \cdot 7H_2O$ (Samchun Chemical, Korea) were dissolved in deionized water in stoichiometric ratio. A homogeneously mixed solution (Ni:Co = 90:10 in molar ratio) and a solution of NaOH (Samchun Chemical, Korea) and NH_4OH (Junsei, Japan) were pumped into a batch reactor (47 L) containing deionized water. The reactor was consistently purged with N_2 gas to remove O_2 in the solution. The precursor powder was finally obtained after washing, filtering, and vacuum drying at 110 °C for 24 h. To obtain NCA89, the precursor $[Ni_{0.9}Co_{0.10}](OH)_2$ was mixed with $LiOH \cdot H_2O$ and $Al(OH)_3$ (Li:(Ni+Co+Al) = 1.01:1, Al/(Ni+Co+Al) = 0.015 in molar ratio) and calcined at 730 °C for 10 h under flowing O_2.

Similarly, Spherical $[Ni_{0.9}Co_{0.09}W_{0.01}](OH)_2$ precursor was synthesized by a coprecipitation method. A homogeneously mixed metal sulfate solution and a solution dissolving WO_3 (Sigma-Aldrich, US), NaOH (Samchun Chemical, Korea), and NH_4OH (Junsei, Japan) were separately pumped into a batch reactor (47 L) containing deionized water. The reactor was consistently purged with N_2 gas to remove O_2 in

the solution. The precursor powder was finally obtained after washing, filtering, and vacuum drying at 110 °C for 24 h. To obtain NCW90, the precursor $[Ni_{0.9}Co_{0.09}W_{0.01}](OH)_2$ was mixed with $LiOH \cdot H_2O$ (Li:(Ni+Co+W) = 1.01:1 in molar ratio) and calcined at 750 °C for 10 h under flowing O_2.

Characterization: The chemical compositions of the cathode powders were measured using inductively coupled plasma (OPIMA 8300, Perkin Elmer). Powder XRD measurements were performed with synchrotron radiation on the 9B-HRPD beamline (λ = 1.51670 Å) at Pohang Accelerator Laboratory (PAL) in Pohang, Korea. The synchrotron XRD profiles were collected in the 2θ range 10°–130° at a 0.01° step size at room temperature with a six-multidetector system. The structural refinement was performed by Rietveld refinement using the Fullprof suite.[24] In situ XRD measurements were performed at the 6D Ulsan National Institute of Science and Technology beamline at PAL in Pohang, Korea. The wavelength of the incident beam was 0.65303 Å and the sample-to-detector distance was calibrated using a CeO_2 standard. A modified coin-type half-cell having a 3 mm hole at its center sealed with a kapton tape served as the X-ray beam path. During charging the modified cell by applying a constant current of 36 mA g^{-1}, the XRD profile was recorded every 3.5 min with a 2D detector (Rayonix MX225-HS) in transmission mode. The 2θ angles from synchrotron beam source for in situ XRD profiles were converted to those from a conventional X-ray tube with λ = 1.5406 Å (Cu K_α radiation) for easy comparison. The morphologies and structures of the prepared cathode were observed by SEM (Verios G4UC, Thermo Fisher Scientific). To observe the cross-section of the secondary particles by SEM, the recovered cathodes at 4.3 V were washed sufficiently using dimethyl carbonate and dried under vacuum in a glovebox. The electrodes were cut using a cross-sectional polisher (IB-19520CCP, JEOL). For the TEM samples, a particle was cut into less than 100 nm thick thin film using a focused ion beam (JEM 2100F, JEOL) and loaded onto a Mo grid. To measure thermal stability, 2032 coin-type half-cells were charged at 4.3 V versus Li metal anode and disassembled for recovering the cathodes in an Ar-filled dry box. The electrodes were rinsed with dimethyl carbonate and dried. Active materials were scraped from the electrodes and packed in stainless steel with gold-plated copper pan. The DSC measurements (DSC 214 polyma, Netzsch, Germany) were performed using 7 mg of active materials with 200 μL fresh electrolyte solution (1.2 mol L^{-1} $LiPF_6$ in ethylene carbonate-ethyl methyl carbonate (EC:EMC = 3:7 by volume) with 2 wt% vinylene carbonate (VC)) at a temperature scan rate of 5 °C min^{-1}.

Electrochemical Test: Each active cathode was homogenized with carbon black and poly(vinylidene fluoride) at a weight ratio of 90:5.5:4.5 in N-methyl pyrrolidone to form a slurry. The slurry was coated onto Al foil with an active material loading of 4 – 5 mg cm^{-2}, roll pressed, and vacuum dried. The electrolyte was 1.2 mol L^{-1} $LiPF_6$ in EC:EMC (= 3:7 by volume) with 2 wt% VC. Electrochemical tests were conducted using 2032 coin-type half-cells with Li metal as the anode. For cycling test, a constant current density was applied by 90 mA g^{-1} (0.5 C-rate) at 30 °C between 2.7 and 4.3 V. Long-term cycling test was performed using laminated-pouch-type full-cells and the mesocarbon-microbead graphite (MCMB, Osaka Gas) as an anode, and 1.2 mol L^{-1} $LiPF_6$ in EC:EMC (= 3:7 by volume) with 2 wt% VC. A N/P ratio for full-cell was in the range of 1.15–1.20. The full-cells were cycled between 3.0 and 4.2 V with a constant 1 C current density (200 mA g^{-1}) at 25 °C. Electrochemical impedance spectroscopy was investigated at charged to 4.3 V using a multichannel potentiostat (VMP3, Bio-Logics) in the range from 1 MHz to 1 mHz.

Supporting Information

Supporting Information is available from the Wiley Online Library or from the author.

Acknowledgements

**ADVANCED
SCIENCE NEWS**

www.advancedsciencenews.com

**ADVANCED
ENERGY
MATERIALS**

www.advenergymat.de

Conflict of Interest

The authors declare no conflict of interest.

Keywords

[1] K. B. Naceur, *Tracking Clean Energy Progress*, International Energy Agency, Paris, France **2016**.

[2] Y. Zhou, T. Stephens, E-Drive Vehicle Sales Analyses: Vehicle Technologies Annual Merit Review, Project VAN011, Argonne National Laboratory, **2014**.

[3] D. Andre, S.-J. Kim, P. Lamp, S. F. Lux, F. Maglia, O. Paschos, B. Stiaszny, *J. Mater. Chem. A* **2015**, *3*, 6709.

[4] S.-T. Myung, F. Maglia, K.-J. Park, C. S. Yoon, P. Lamp, S.-J. Kim, Y.-K. Sun, *ACS Energy Lett.* **2017**, *2*, 196.

[5] A. Manthiram, J. C. Knight, S.-T. Myung, S.-M. Oh, Y.-K. Sun, *Adv. Energy Mater.* **2016**, *6*, 1501010.

[6] Y. Ding, Z. P. Cano, A. Yu, J. Lu, Z. Chen, *Electrochem. Energy Rev.* **2019**, *2*, 1.

[7] Y. Miao, P. Hynan, A. v. Jouanne, A. Yokochi, *Energies* **2019**, *12*, 1074.

[8] Tesla Motors, https://www.tesla.com/models (accessed: July 2019).

[9] K.-S. Lee, S. T. Myung, K. Amine, H. Yashiro, Y.-K. Sun, *J. Electrochem. Soc.* **2007**, *154*, A971.

[10] J. Shim, R. Kostecki, T. Richardson, X. Song, K. A. Striebel, *J. Power Sources* **2002**, *112*, 222.

[11] S.-M. Bak, E. Hu, Y. Zhou, X. Yu, S. D. Senanayake, S.-J. Cho, K.-B. Kim, K. Y. Chung, X.-Q. Yang, K.-W. Nam, *ACS Appl. Mater. Interfaces* **2014**, *6*, 22594.

[12] C. S. Yoon, M. H. Choi, B.-B. Lim, E.-J. Lee, Y.-K. Sun, *J. Electrochem. Soc.* **2015**, *162*, A2483.

[13] H.-J. Noh, S. Youn, C. S. Yoon, Y.-K. Sun, *J. Power Sources* **2013**, *233*, 121.

[14] U.-H. Kim, D.-W. Jun, K.-J. Park, Q. Zhang, P. Kaghazchi, D. Aurbach, D. T. Major, G. Goobes, M. Dixit, N. Leifer, C. M. Wang, P. Yan, D. Ahn, K.-H. Kim, C. S. Yoon, Y.-K. Sun, *Energy Environ. Sci.* **2018**, *11*, 1271.

[15] H.-H. Ryu, G.-T. Park, C. S. Yoon, Y.-K. Sun, *J. Mater. Chem. A* **2019**, *7*, 18580.

[16] R. D. Shannon, *Acta Crystallogr. A* **1976**, *32*, 751.

[17] S. Watanabe, M. Kinoshita, T. Hosokawa, K. Morigaki, K. Nakura, *J. Power Sources* **2014**, *258*, 210.

[18] S. Watanabe, M. Kinoshita, T. Hosokawa, K. Morigaki, K. Nakura, *J. Power Sources* **2014**, *260*, 50.

[19] T. Ohzuku, A. Ueda, M. Nagayama, *J. Electrochem. Soc.* **1993**, *140*, 1862.

[20] C. S. Yoon, D.-W. Jun, S.-T. Myung, Y.-K. Sun, *ACS Energy Lett.* **2017**, *2*, 1150.

[21] H.-H. Ryu, K.-J. Park, C. Yoon, Y.-K. Sun, *Chem. Mater.* **2018**, *30*, 1155.

[22] C. S. Yoon, H.-H. Ryu, G.-T. Park, J.-H. Kim, K.-H. Kim, Y.-K. Sun, *J. Mater. Chem. A* **2018**, *6*, 4126.

[23] A. Ovid'ko, *Philos. Trans. R. Soc., A* **2015**, *373*, 20140129.

[24] Fullprof Manual, https://www.ill.eu/sites/fullprof (accessed: August 2019).